WILEY-VCH

DOI: 10.1002/ ((please add manuscript number))
Full Paper

In Situ Structure Characterization in Slot-Die Printed All-Polymer Solar Cells with Efficiency Over 9%

Wenkai Zhong, Qin Hu, Yufeng Jiang, Yu Li, Teresa L. Chen, Lei Ying, Feng Liu,* Cheng Wang, Yi Liu, Fei Huang,* Yong Cao, Thomas P. Russell**

W. Zhong, Prof. L. Ying, Prof. F. Huang, Prof. Y. Cao
Institute of Polymer Optoelectronic Materials and Devices, State Key Laboratory of Luminescent Materials and Devices, South China University of Technology, Guangzhou 510640, P. R. China
E-mail: msleiying@scut.edu.cn; msfhuang@scut.edu.cn

Dr. Y. Li, Prof. F. Liu
Department of Physics and Astronomy and Collaborative Innovation Center of IFSA (CICIFSA), Shanghai Jiao Tong University, Shanghai 200240, P. R. China
E-mail: fengliu82@sjtu.edu.cn

W. Zhong, Dr. C. Wang
Advanced Light Source, Lawrence Berkeley National Laboratory, Berkeley, CA 94720, United States

Y. Jiang, Dr. Y. Li, Dr. Q. Hu, Prof. T. P. Russell
Materials Science Division, Lawrence Berkeley National Laboratory, Berkeley, CA 94720, United States
E-mail: tom.p.russell@gmail.com

T. L. Chen, Dr. Y. Liu
The Molecular Foundry, Lawrence Berkeley National Laboratory, Berkeley, CA 94720, United States

Dr. Q. Hu, Prof. T. P. Russell
Department of Polymer Science and Engineering, University of Massachusetts, Amherst, Massachusetts 01003, United States

Abstract: In this study, we demonstrate high-performance printed all-polymer solar cells based on bulk-heterojunction (BHJ) blend film using PTzBI as the donor and N2200 as the acceptor. A slot-die process was utilized to prepare the BHJ blend, which is a cost-effective, high-throughput approach to achieve large-area photovoltaic devices. The real-time crystallization of polymers in the film drying process was investigated by *in situ* grazing incidence wide-angle X-ray scattering characterization. Printing was found to significantly improve crystallinity of the polymer blend in comparison to spin-coating. Moreover, printing with 1,8-diiodooctance as the solvent additive enhanced the polymer aggregation and crystallization during solvent evaporation, eventually leading to multi-length-scale phase separation, with PTzBI-rich domains in-between the N2200 crystalline fibers. This unique morphology achieved by printing fabrication resulted in an impressively high power conversion efficiency of 9.10%, which is the highest efficiency for reported printed all-polymer solar cells. These findings provide important guidelines for controlling film drying dynamics for processing all-polymer solar cells.

1. Introduction

Thin film organic photovoltaic (OPV) devices have attracted great interest from both the academic and industrial communities due to their lightweight, high flexibility, and amenability to cost-effective roll-to-roll fabrication. Recently, the overall photovoltaic performance of OPV devices has significantly increased due to the rapid progress of new photoactive materials and advanced device engineering.[1-7] However, a major obstacle for the rapid expansion of the OPV sector is that most of the reported highly efficient devices are prepared by spin-coating, where ~90% of the material is lost and the kinetic processes, including solvent evaporation, crystallization and phase separation, are far different than printing processes used on a commercial level. Consequently, it is difficult, if not impossible, to extrapolate results from spin-coated materials to active layers used for device fabrication. One effective strategy to address this issue is to use printing techniques, such as doctor blading, slot-die coating, or ink

jet printing that are high-throughput, material-efficient (99% of material retrieved), and are very compatible with the large-area production.[8-10] Unlike spin-coating, the solvent removal rate in thin film printing is slower, and, therefore, can allow for the formation of more ordered crystalline domains. The kinetic pathways of thin film printing are more likely to promote the formation of large aggregated domains, while spin-coating kinetic processes are arrested at an earlier stage due to rapid solvent evaporation. These differences can markedly impact exciton dissociation and charge transport in bulk-heterojunction (BHJ) thin films that dictate optoelectronic processes and determine the power conversion efficiencies (PCEs).[11-13]

All-polymer solar cells (all-PSCs), comprised of a polymer donor and a polymer acceptor, have excellent optical and electrical stability, and specific advantages of mechanical properties that were favorable for long-term operational stability.[14-24] Previous efforts in printing devices based on fullerene derivatives or small molecule acceptors indicated that the photovoltaic performance could be controlled, to some extent, by manipulating the printing conditions.[25-32] However, much less effort has been devoted to all-PSCs primarily due to the lack of an effective strategy to control the intricate morphology during printing.[33-35] Ade and coworkers found that multi-length scale morphology of printed all-polymer blend, could be controlled by the incorporation of solvent additives, but an enhanced multi-length scale phase separation did not positively impact solar cell efficiency.[34] Bao and coworkers found that the P3HT:PNDIT blends showed a strong tendency to phase separate into large domains due to crystallization, which significantly reduced exciton splitting at the donor/acceptor interface.[35] Consequently, the morphology has proven to be the bottleneck in printed all-PSCs development, leading to PCEs far below the highest reported efficiencies (~11%) of spin-coated devices.[36-39]

Control over the morphology of all polymer BHJ films has been achieved via various approaches, including but not limited to, tuning material structures[40-45], altering film processing solvents[46-50], processing with solvent additives[51-53], post treatments for the films[37,54,55], improving film deposition methods[33,56] and so forth.

Here, we fabricated all-PSCs based on an electron-donating polymer PTzBI and an electron-accepting polymer N2200 (the chemical structures shown in Figure 1a) that can be printed from 2-methyltetrahydrofuran (MTHF), an ecofriendly solvent[50], in the presence of a small amount of 1,8-diiodooctane (DIO) as the solvent additive.[57,58] Devices fabricated by slot-die printing showed impressively higher PCEs of 9.10%, the highest efficiencies reported for printed all-PSCs. The superior device performance is attributed to the enhanced crystallization of the polymers and multi-length scale morphology achieved by BHJ film printing with DIO additive.

2. Results and Discussions

To evaluate the solar cell efficiency, a conventional device architecture of ITO/PEDOT:PSS/Active layer/PFN-Br/Ag was used. The active layer consisted of PTzBI and N2200 at a weight ratio of 2:1. MTHF was used as the host solvent and 0.3 vol% DIO was used as the solvent additive to tune the morphological features of the polymer blend. Following deposition, the films were thermally annealed at 120 ºC for 10 min. More details of device fabrication are given in the supporting information (SI). The current density-voltage (*J*-*V*) characteristics of the resultant devices were measured under AM 1.5G illumination (100 mW cm^{-2}) and the external quantum efficiency (EQE) curves are shown in Figure 1. The reference device, processed by spin-coating without DIO, showed an average efficiency of 8.42 ± 0.07%, an open-circuit voltage (V_{OC}) of 0.85 ± 0.01 V, a short-circuit current density (J_{SC}) of 15.2 ± 0.2 mA cm^{-2}, and a fill factor of (*FF*) of 0.65 ± 0.01, very similar to that reported previously.[50] When the polymer blend was processed by spin-coating with DIO, the *FF* dramatically increased to 0.74 ± 0.01, but the J_{SC} dropped, giving a slightly higher PCE of 8.54 ± 0.14%. For blends printed without DIO, the devices showed a PCE of 8.24 ± 0.10%, comparable to the spin-coated devices. For blends printed with DIO, the devices showed a higher *FF* of 0.70 ± 0.01 and maintained a high J_{SC} of 15.2 ± 0.2 mA cm^{-2}, giving a PCE of 8.61 ± 0.12%. Further optimization was carried out by optimizing the DIO volume fraction in the BHJ solution for

printing. Using 0.1% DIO during film printing can further promote the device performance with a maximum PCE of 9.10% (J_{SC} = 15.4 mA cm^{-2}, V_{OC} = 0.84 V, *FF* = 0.70), due to the combination of high *FF* and remained J_{SC}. However, BHJ film printing with 0.5% DIO was found to significantly decline device current density. Detailed photovoltaic parameters are given in Table 1. The different OPV performances suggested significant morphological differences for the PTzBI:N2200 blends prepared by spin-coating and printing, as well as with and without DIO.

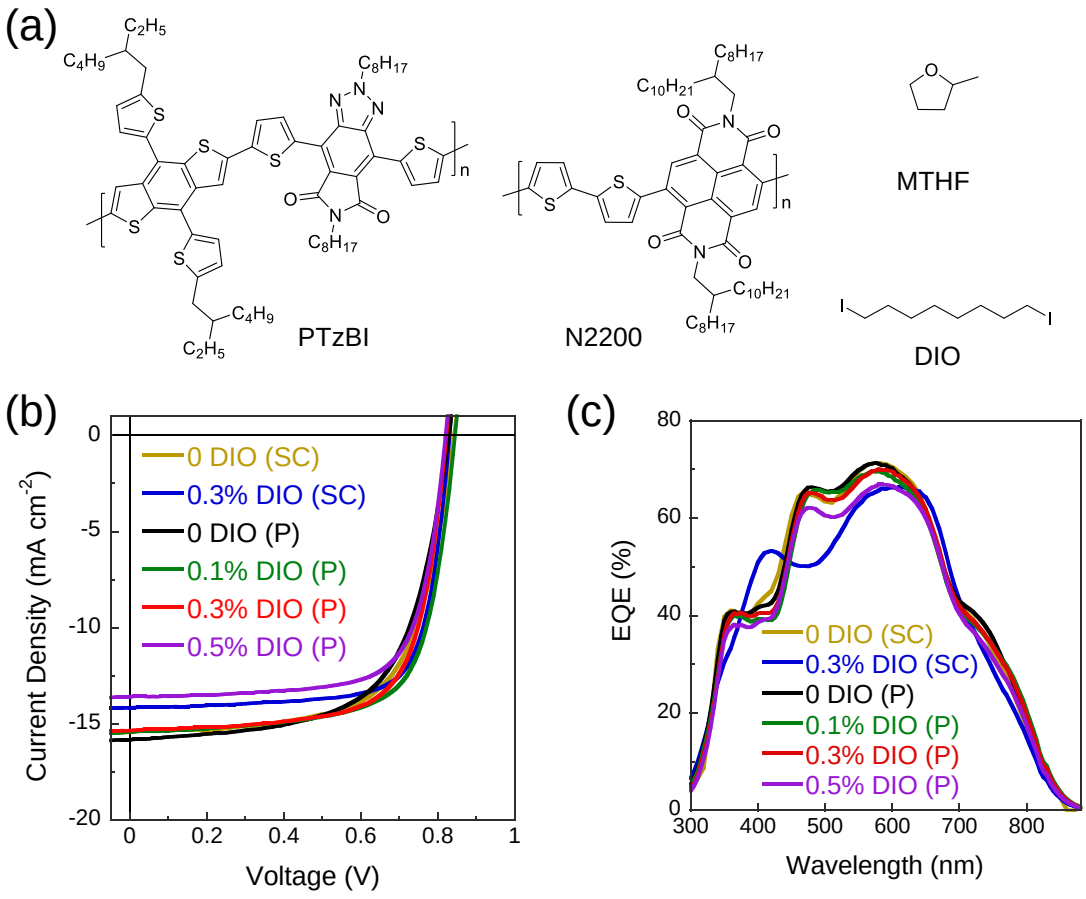

Figure 1. (a) Chemical structures of PTzBI, N2200, MTHF, and DIO; (b) *J-V* characteristics and (c) EQE curves of solar cells processed using spin-coating (SC) and printing (P) methods.

Table 1. Photovoltaic parameters of solar cells based on the PTzBI:N2200 (2:1) BHJ films.

Deposition Method	DIO volume fraction (%)	J_{SC}[a] (mA cm^{-2})	V_{OC}[a] (V)	FF[a]	PCE[a] [PCE^{max}] (%)
spin-coating	0	15.2 ± 0.2	0.85 ± 0.01	0.65 ± 0.01	8.42 ± 0.07 [8.54]
	0.3	13.9 ± 0.2	0.83 ± 0.01	0.74 ± 0.01	8.54 ± 0.14 [8.76]
printing	0	15.5 ± 0.2	0.83 ± 0.00	0.64 ± 0.01	8.24 ± 0.10 [8.34]
	0.1	15.3 ± 0.2	0.83 ± 0.01	0.70 ± 0.01	8.88 ± 0.13 [9.10]
	0.3	15.2 ± 0.2	0.82 ± 0.01	0.70 ± 0.01	8.61 ± 0.12 [8.82]
	0.5	13.5 ± 0.2	0.82 ± 0.01	0.71 ± 0.01	7.89 ± 0.15 [8.02]

[a] The static parameters were averaged from ten separated devices.

PTzBI:N2200 blends are all polymer systems that have multiple crystallization kinetics. To gain an in-depth understanding of the morphology development, *in situ* grazing incidence wide-angle X-ray scattering (GIWAXS) was conducted. The *in situ* experimental setup was similar to our previous report.[26] Figure 2a-d show the GIWAXS line-cut profiles obtained during film drying. Peak fitting results are plotted in Figure 2e-h. It should be noted that PTzBI and N2200 have quite similar lamellae and π-π packing structures that cannot be separated. GIWAXS peak fitting was thus used to evaluate the overall crystalline feature of the blend films. Before discussing the evolution of the morphology, we distinguish three different periods during the drying process: I. dissolution, II. nucleation and rapid growth, III. trace solvent evaporation and crystallinity stabilization, according to the trend in the change in peak areas, which are indicated in Figure 2e-h. For blend films processed without DIO, in period I, the polymers are fully dissolved without any scattering signatures. The scattering from MTHF showed a broad isotropic diffraction rings centered at q ~ 1.3 Å^{-1} (Figure S2 and S3, SI). In period II (~1.2 s), with the solvent evaporation, the polymers reach the solubility in the MTHF and nuclei form, followed by rapid

crystallite growth. During this time, reflections characteristic of crystallization, including the (010) π-π stacking peak in the out-of-plane (OOP) direction, and the (100) lamellar stacking peak in the in-plane (IP) direction appeared and rapidly increased in intensity. The *d*-spacings decreased (from 3.65 to 3.56 Å for the π-π stacking and from 26.8 to 23.1 Å for the lamellar stacking), and the reflections sharpened along with a corresponding increase in the crystal coherence length (CCL) and the integrated peak area. The rapid drying ends after ~5.1 s, followed by trace solvent removal and crystallinity stabilization, i.e. period III. During period III, with further evaporation of the residual MTHF, crystallization improved as indicated by the consecutive increase in the peak area, and finally, the crystals stabilized as the solvent fully removed. It is interesting to note that the evolution of (010) and (100) peak are similar. The *d*-spacing of the (001) reflection, arising from intramolecular electron density correlations, was constant. These results suggest that intermolecular interactions are enhanced during solvent removal through alkyl-alkyl interactions and π-π stacking. The initial packing is ill-defined, affording space for cooperative chain reorganization, which led to the changes in the (100) and (010) Bragg spacings and changes in the CCL of the (001) reflection.

The addition of DIO leads to a significant change in the thin film morphology. MTHF is a volatile solvent (78-80 ^{o}C), and DIO has a high boiling point (327 ^{o}C).[59] Thus, DIO remains in the film much longer than MTHF. For blend film processed with DIO, the (010) peak in the OOP direction was difficult to fit due to overlap with the DIO signal that emerged at ~1.5 Å^{-1}. The evolution of the (100) peak in the IP direction is quite distinct. A similar crystallization behavior was seen during the early state of drying (periods I and II). However, adding DIO into MTHF prolonged the emergence of polymer crystals, and period II appeared after ~6.0 s. The reduction in *d* spacing is also much smaller when compared to that seen with only MTHF processing, indicating the presence of DIO perturbs the long-range interaction of the polymer chains. In region II, the CCL increased more than that observed for the wet-film without DIO. Thus, better crystal packing can be obtained. We note that the

diffraction peak area or intensity significantly decreases in the wet-film with DIO in comparison to that in the film without DIO. This can be attributed to two major reasons: (1) the presence of DIO that retards crystallization; (2) the absorption of the DIO. Since the absorption of DIO is much greater than the polymer (Figure S4), the diffraction intensity will be less. Due to the slow evaporation of DIO, the (010) peak in the OOP direction was not discernable even after ~18 s. Thermal annealing was used to completely dry the film. Consequently, the presence of DIO significantly altered the evolution of the morphology. The much-improved CCL of the (100) peak indicates that high quality polymer crystals can be obtained. It is expected that the conformation of the solubilizing side chains of the polymer are extended when DIO is present, thus a better chain locking is achieved in (100) direction when the thin film was fully dried. The absence of the (001) reflection indicates a lack of correlations along the chain axis which may reflect a conformational disorder induced by the interactions of the chain with DIO.

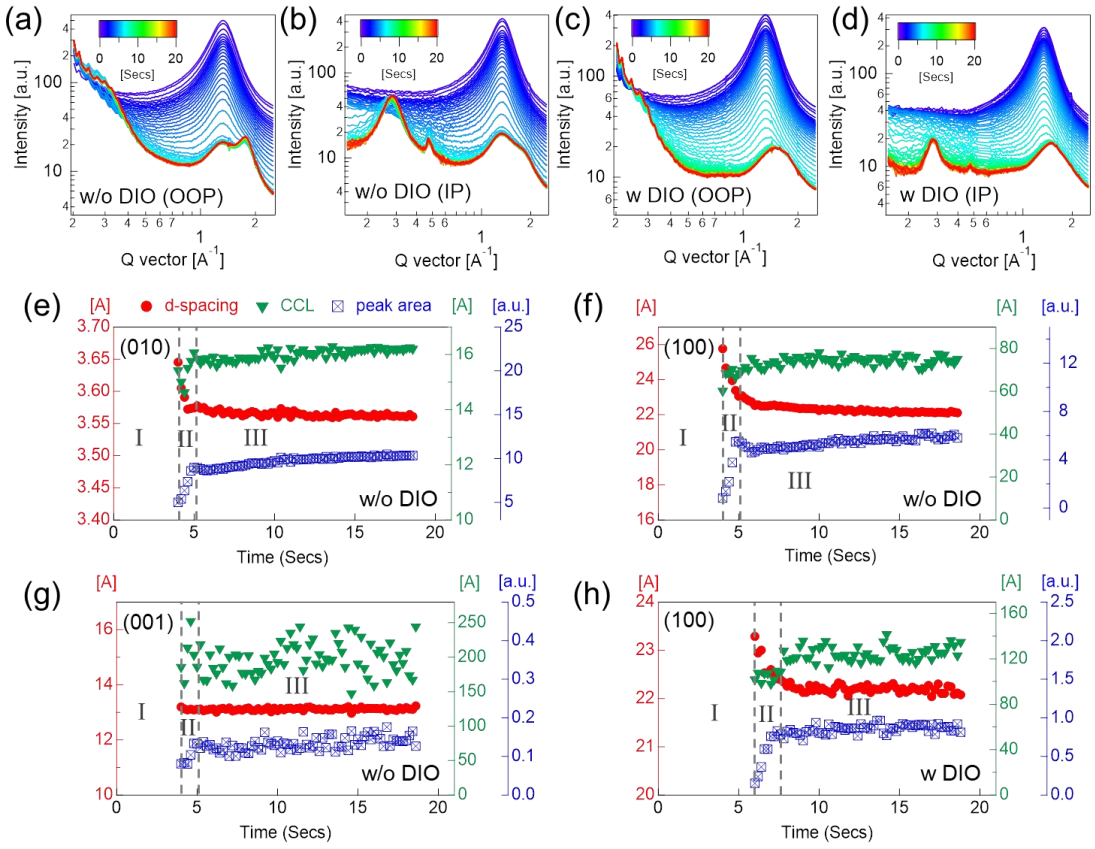

Figure 2. *In situ* GIWAXS line-cut profiles of PTzBI:N2200 blend wet-film drying process (a,b) with (w) or (c,d) without (w/o) DIO; analysis of in situ GIWAXS results: (e) (010) peak, (f) (100) peak, and (g) (001) peak of the wet-film without DIO; (h) (100) peak of the wet-film with DIO.

Figure 3 shows the final GIWAXS two dimensional (2D) diffraction patterns, lint-cut profiles, and CCL analysis of the PTzBI:N2200 thin films prepared by the different processes. The pristine thin films are also characterized and the results are provided in Figure S5. The PTzBI shows a (100) diffraction at q = 0.29 Å^{-1} in the IP direction, and a (010) peak at 1.76 Å^{-1} in the OOP direction. The crystallinity of the N2200 is evident, with a (010) peak at 1.61 Å^{-1} in the OOP, as well as the (100) (0.26 Å^{-1}) and (001) (q = 0.47 Å^{-1}) peaks in the IP direction. Thus, both conjugated backbones of the polymers prefer a face-on orientation. The (010) π-π stacking peak and (100) lamellar stacking features for the blend films are an additive combination of each component. In BHJ films, these 4 samples showed similar diffraction features. In general, adding DIO into the processing solution enhances the CCLs of the (100) and (001) reflections, during transition from solution to the dried state. The directly printed thin film shows a week (001) peak, indicating poor electron density correlations along the chain axis. Therefore, it is quite important to remove the DIO after film printing and to thermally anneal subsequently. DIO is a high boiling point liquid that can swell or reside within the BHJ thin films, its slow removal, in comparison to MTHF, could lead to a much improved structural order of the BHJ thin films, wherein the CCL of the (100) can increase up to several tens of nanometers. The DIO swelled thin film has a larger (100) CCL in comparison to the fully dried thin film, indicating that the removal of the DIO disrupts the interchain packing. The chain packing achieved with printing is enhanced over that seen with spin-coated films, as evidenced by the increase in the CCLs of the (100) and (001) reflections. This, more than likely, arises from the slower drying kinetics, affording more time for chain reorganization and ordering during film drying. The (100) peak intensities of

these four blends were also investigated. To understand the behavior of the peak intensities of the film processed with and without DIO, line-cut profiles in the high *q* region (~2.6 $Å^{-1}$) were normalized (Figure S6). In this region, there is no structural information and the scattering arises primarily from thermal density fluctuations and incoherent scattering. We assumed this was similar for all the samples investigated. For the spin coated samples, the addition of DIO was found to decrease the (010) peak intensity, but showed no effects on the (100) intensities. However, with the printed sample, DIO was found to significantly enhance the both (010) and (100) intensities, indicating an increase in the crystallinity. The enhanced peak intensities for the film printed with DIO after drying may arise from the removal of the DIO during thermal annealing. These results indicate that the different drying procedures afforded by printing can lead to an enhancement of the crystallinity or more ordered structures within the film. The improved structural order of both PTzBI and N2200, enabled by using printing with the use of DIO as an additive, also parallels the improved charge transport in the blend films, leading to the significant increase in the device *FF*.

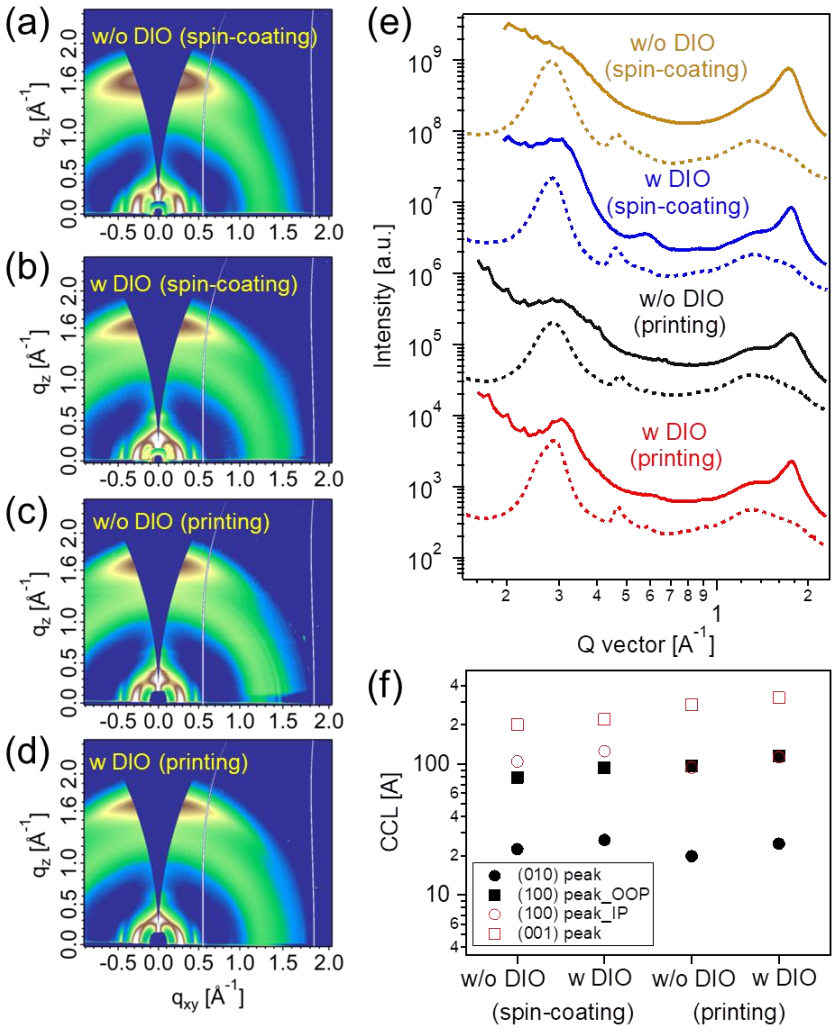

Figure 3. (a-d) GIWAXS 2D patterns of the PTzBI:N2200 blends; (e) OOP (solid lines) and IP (dashed lines) line-cut profiles of the GIWAXS 2D patterns; (f) Summary of CCLs for the blends.

Transmission electron microscopy (TEM) was used to image the morphology of the blend films in real space (Figure 4). The TEM image of PTzBI:N2200 blend film spin-coated without DIO showed a fiber-like structure (bright regions) throughout the entire film, which can be attributed to the N2200 crystalline aggregates.[60] These fibrils became finer when the film was processed with DIO. Such a delicate fibrillar structure facilitates charge transport in the blend films, one of the origins of the drastic *FF* improvement in the resultant devices. The blend film printed without DIO showed similar fibrillar features but with slightly larger fibrils when compared to the

spin-coated films, since the drying during printing is slower, affording more time for polymer chains to order. For the blend films printed with DIO, a mesh-like fibrillar structures is seen. The film also appears coarser when compared to films printed without DIO, since DIO not only induces polymer packing but also aggregation; this leads to a multi-length scaled morphology. The dark regions in the micrograph arise from the PTzBI-rich domains containing the crystalline and amorphous phase, whereas the N2200 crystalline fibrils are distributed in the PTzBI-rich domains boundaries. Resonant soft X-ray scattering (RSoXS) was performed to determine a statistical average of the domain size of the blend films. The contrast function of the PTzBI:N2200 film can be calculated from the near edge X-ray absorption fine structure (NEXAFS) spectra of the neat films (Figure S7, SI). Based on the contrast function, RSoXS patterns and sector averaged profiles (90^{o} and 180^{o}) were taken at a photon energy of 285.0 eV at the carbon K-edge (Figure 5), which is sensitive to the polymer 1s-$\pi^*_{C=C}$ bond transition. When spin-coated without DIO, the profile of the blend film showed a broad, diffuse shoulder at ~0.006 Å^{-1}, corresponding to a domain size of ~105 nm. This broad peak shifted to ~0.007 Å^{-1} (~90 nm) when the blend was processed by printing. Thus, while printing leads to an improved fibrillar structure formation, it reduces the domain size characteristic of the phase separated morphology. This is paralleled with an improved *J*sc in the solar cell device. For blend films processed with DIO, anisotropy in the RSoXS was seen in the 2D patterns, which became more evident for the printed films. For the blend films printed with DIO, a broad reflection at ~0.0062 Å^{-1} (~100 nm) was observed, and a weak reflection at ~0.011 Å^{-1} (~57 nm) appeared, indicative of the formation of a multi-length-scale morphology. The large scale interference is ascribed to the domain size of the PTzBI-rich domains, while the shorter length scale interference arises from the N2200 fibril-to-fibril distance. The anisotropy in the pattern indicates that the N2200 fibril axis was parallel to the domains.[61,62]

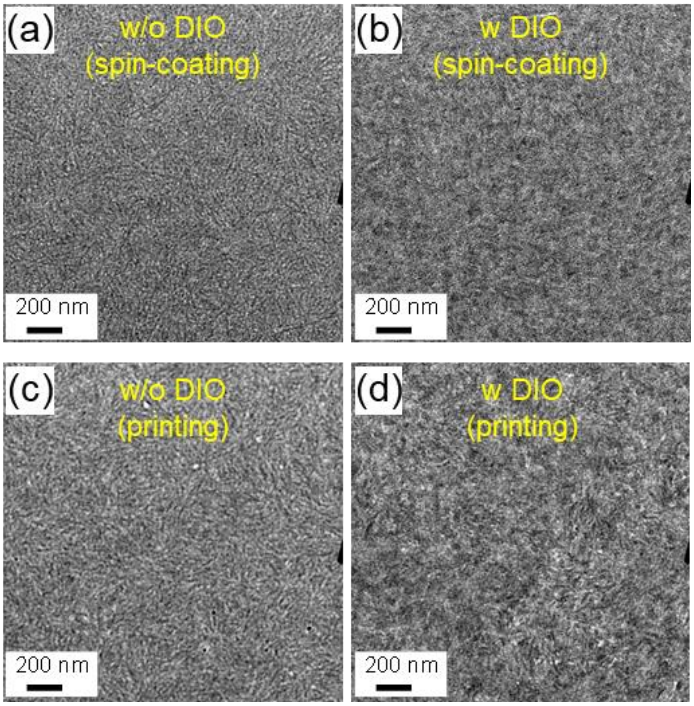

Figure 4. TEM images of PTzBI:N2200 blends processed by spin-coating and printing.

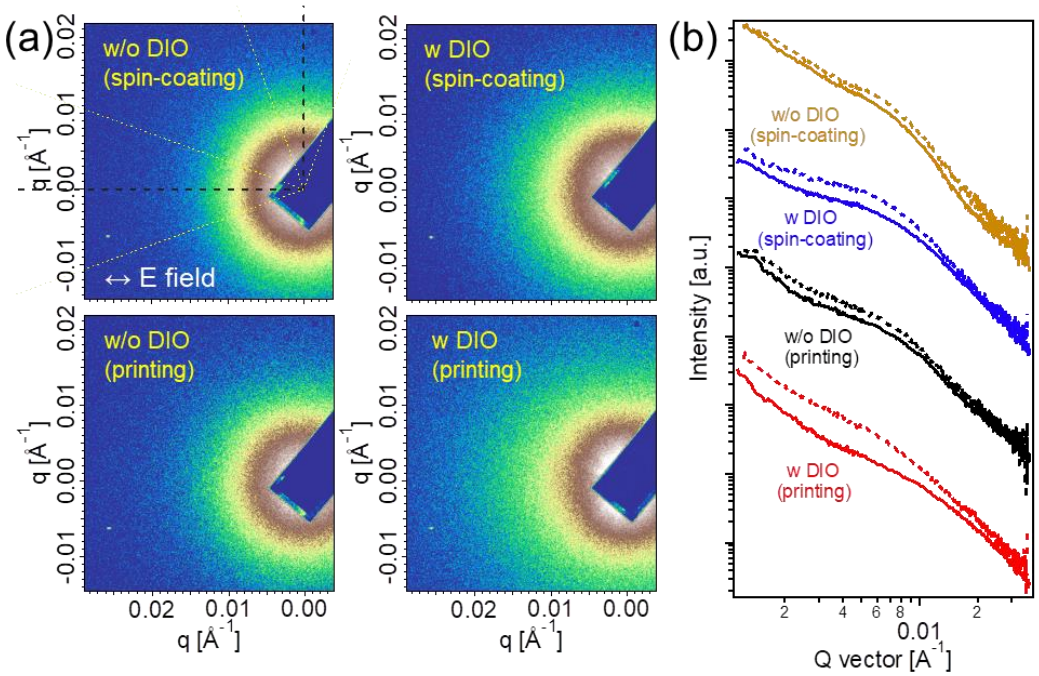

Figure 5. RSoXS (a) 2D patterns and (b) corresponding sector averaged profiles (dashed line: 90°; solid line:180°) of PTzBI:N2200 blends processed by spin-coating and printing.

The morphological structures of BHJ films are highly correlated to the charge transport, recombination, and collection inside the all-PSCs. By plotting V_{OC} as a function of the log of the light intensity (P_{light}) (Figure S9, SI), the extracted slopes are 1.32 and 1.15 kT/q for devices spin-coated without and with DIO, respectively, while 1.52 and 1.24 kT/q for devices printed without and with DIO, respectively. The lower slope of BHJ films coated with DIO suggests a weaker Shockley-Read-Hall recombination, indicative of decreased traps of each domain.[46,63] By using charge collection probability (P_C) with respect to effective voltage (V_{eff}) in the low voltage region (Figure S10, SI), the devices printed with DIO show a higher P_C of 83.1% / 96.8% than those printed without DIO (77.4% / 95.4%) at the max-power / short-circuit condition, reflecting an overall improved efficiency of exciton splitting and charge collection. To get insight charge transport in the BHJ films, charge-only devices were fabricated to extract the vertical charge mobilities by space-charge-limited current (SCLC) method (Figure S11 and Table S1, SI). The addition of DIO in BHJ solution shows different impacts on the electron (μ_h) and hole (μ_e) mobilities of the resultant thin films. For spin-coating, DIO is helpful to the formation of fibrillar structures that stem from N2200 crystallite aggregations. The N2200 fibers provide the electron transport channels in the entire BHJ film, leading to the enhanced μ_e from 3.26×10^{-5} to 4.76×10^{-5} cm^2 V s. However, spin-coating with DIO is also found to significantly decrease the μ_h of the films, from 8.85×10^{-4} to 1.37×10^{-4} cm^2 V s. We attribute the lower J_{SC} for the devices processed by spin-coating with DIO to the drastically decreased μ_h due to the N2200 fibers in-between the PTzBI-rich domains that partially disrupt the hole transport channels. Similar to spin-coating, BHJ films printed with DIO also shows increased μ_e from 3.37×10^{-5} to 8.32×10^{-5} cm^2 V s, but decreased μ_h from 1.00×10^{-3} to 5.51×10^{-4} cm^2 V s, in comparison to the as cast BHJ films. Thanks to the more order structures in printed films, the μ_h does not drop significantly and thus the slightly decreased J_{SC}. Meanwhile, as shown in J_{ph}-V_{eff} characteristics (Figure S10, SI), the device printed with DIO shows a slightly lower saturated J_{ph} than that of the device printed without

DIO, indicating the lower efficiency of the exciton dissociation process. Consequently, despite the traps inside the BHJ blend are decreased, the exciton dissociation and hole transport are not highly improved, leading to the slightly decreased J_{SC}. However, the combination of enhanced μ_e and decreased μ_d affords the electron/hole transport balance, giving an increased *FF* for device processed with DIO. Therefore, the multi-length scale morphology coupled with fibrillar structures that generated by printing with DIO is advantageous in suppressing charge recombination and promoting the balance for charge transport. These factors lead to the significantly increased device *FF* and efficiency.

Collectively, the GIWAXS, TEM, and RSoXS provide insight into the evolution of the PTzBI:N2200 blend film morphology during printing without or with DIO. Initially, both polymers are solubilized with pre-aggregation in MTHF regardless of any additive.[50] For blend film processed without DIO, as the MTHF evaporates, the concentrations of the polymers increase and they begin to crystallize. The crystals grow rapidly and phase-separation occurs, with the continued evaporation of the residual solvent, the ordering improves, as evidenced by the decreased *d*-spacings and the increased CCLs, and the increase in the peak area. For blend film processed with DIO, when most of the MTHF is removed, a rapid crystallization of the polymers and the initial stages of phase separation occur, similar to that seen without DIO. With concentration increasing of the non-solvent DIO, both PTzBI and N2200 show enhanced aggregation and continues to crystalize. The chain packing of the PTzBI improves forcing N2200 to the boundaries, whereas the ordering of the N2200 improves, forming fibrils that surround the PTzBI-rich domains, leading to the formation of a multi-length-scale morphology.

3. Conclusion

In conclusion, printed PTzBI:N2200 blends exhibit higher photovoltaic efficiencies than films processed by spin-coating. The printing process facilitates the

crystallization of the polymers that leads to an increase in the current density of resultant device. The DIO additive enhances polymer aggregation when most of the host solvent MTHF has evaporated. These aggregates ultimately lead to a fibrillar network morphology and form a smaller length-scale structure relative to the domain size of the network. The combination of the improved order and formation of a multi-length-scale phase separation of the MTHF/DIO printed PTzBI:N2200 blends decreases the trap-assisted charge recombination and promotes the charge transport balance, as well as the efficiency of charge generation and collection, giving a power conversion efficiency of 9.10%, which is the highest efficiency of printed all-polymer solar cells reported to date. The results presented here afford an understanding of the film deposition process and the role of solvent additives on the crystallization and phase separation of the polymer blend, opening a pathway for large-area processing of all-polymer solar cells.

Supporting Information

Supporting Information is available from the Wiley Online Library or from the author.

Notes

The authors declare no competing financial interest.

Acknowledgements

W. Zhong and Q. Hu contributed equally. This work was financially supported by the National Natural Science Foundation of China (No. 21822505, 21520102006, 51521002 and 51673069). TPR and QH were supported by the US Office of Naval Research under contract N00014-17-1-2244. This research used the resources of beamline 7.3.3 and 11.0.1.2 at Advanced Light Source, Materials Science Division, The Molecular Foundry, Lawrence Berkeley National Laboratory, which was

supported by the Office of Science, Office of Basic Energy Sciences, of the U.S. Department of Energy under Contract No. DE-AC02-05CH11231.

Received: ((will be filled in by the editorial staff))

Revised: ((will be filled in by the editorial staff))

Published online: ((will be filled in by the editorial staff))

References

[1] L. X. Meng, Y. M. Zhang, X. J. Wan, C. X. Li, X. Zhang, Y. B. Wang, X. Ke, Z. Xiao, L. M. Ding, R. X. Xia, H. L. Yip, Y. Cao, Y. S. Chen, Science **2018**, 361, 1094.

[2] X. Z. Che, Y. X. Li, Y. Qu, S. R. Forrest, *Nat. Energy* **2018**, *3*, 422.

[3] Z. Zheng, Q. Hu, S. Q. Zhang, D. Y. Zhang, J. Q. Wang, S. K. Xie, R. Wang, Y. P. Qin, W. N. Li, L. Hong, N. N. Liang, F. Liu, Y. Zhang, Z. X. Wei, Z. Y. Tang, T. P. Russell, J. H. Hou, H. Q. Zhou, *Adv. Mater.* **2018**, *30*, 1801801.

[4] Z. C. Zhou, S. J. Xu, J. N. Song, Y. Z. Jin, Q. H. Yue, Y. H. Qian, F. Liu, F. L. Zhang, X. Z. Zhu, *Nat. Energy* **2018**, *3*, 952.

[5] Y. Cui, H. F. Yao, C. Y. Yang, S. Q. Zhang, J. H. Hou, *Acta. Polym. Sin.* **2018**, 223.

[6] J. H. Hou, O. Inganas, R. H. Friend, F. Gao, *Nat. Mater.* **2018**, *17*, 119.

[7] P. Cheng, G. Li, X. W. Zhan, Y. Yang, *Nat. Photonics* **2018**, *12*, 131.

[8] F. C. Krebs, *Sol. Energy Mat. Sol. C.* **2009**, *93*, 394.

[9] X. D. Gu, L. Shaw, K. Gu, M. F. Toney, Z. N. Bao, *Nat. Commun.* **2018**, *9*, 534.

[10] T. R. Andersen, H. F. Dam, M. Hosel, M. Helgesen, J. E. Carle, T. T. Larsen-Olsen, S. A. Gevorgyan, J. W. Andreasen, J. Adams, N. Li, F. Machui, G. D. Spyropoulos, T. Ameri, N. Lemaitre, M. Legros, A. Scheel, D. Gaiser, K. Kreul, S. Berny, O. R. Lozman, S. Nordman, M. Valimaki, M. Vilkman, R. R. Sondergaard, M. Jorgensen, C. J. Brabec, F. C. Krebs, *Energy Environ. Sci.* **2014**, *7*, 2925.

[11] A. Teichler, R. Eckardt, S. Hoeppener, C. Friebe, J. Perelaer, A. Senes, M. Morana, C. J. Brabec, U. S. Schubert, *Adv. Energy Mater.* **2011**, *1*, 105.

[12] F. Liu, Y. Gu, C. Wang, W. Zhao, D. Chen, A. L. Briseno, T. P. Russell, *Adv. Mater.* **2012**, *24*, 3947.

[13] F. Liu, Y. Gu, X. B. Shen, S. Ferdous, H. W. Wang, T. P. Russell, *Prog. Polym. Sci.* **2013**, *38*, 1990.

[14] S. H. Shi, J. Y. Yuan, G. Q. Ding, M. Ford, K. Y. Lu, G. Z. Shi, J. X. Sun, X. F. Ling, Y. Li, W. L. Ma, *Adv. Funct. Mater.* **2016**, *26*, 5669.

[15] Y. N. Zhang, Y. L. Xu, M. J. Ford, F. C. Li, J. X. Sun, X. F. Ling, Y. J. Wang, J. N. Gu, J. Y. Yuan, W. L. Ma, *Adv. Energy Mater.* **2018**, *8*, 1800029.

[16] J. W. Jung, J. W. Jo, C. C. Chueh, F. Liu, W. H. Jo, T. P. Russell, A. K. Y. Jen, *Adv. Mater.* **2015**, *27*, 3310.

[17] M. Liu, J. Yang, Y. L. Yin, Y. Zhang, E. J. Zhou, F. Y. Guo, L. C. Zhao, *J. Mater. Chem. A* **2018**, *6*, 414.

[18] Y. J. Hwang, B. A. E. Courtright, A. S. Ferreira, S. H. Tolbert, S. A. Jenekhe, *Adv. Mater.* **2015**, *27*, 4578.

[19] Z. G. Zhang, Y. K. Yang, J. Yao, L. W. Xue, S. S. Chen, X. J. Li, W. Morrison, C. Yang, Y. F. Li, *Angew. Chem. Int. Edit.* **2017**, *56*, 13503.

[20] Y. K. Guo, Y. K. Li, O. Awartani, H. Han, J. B. Zhao, H. Ade, H. Yan, D. H. Zhao, *Adv. Mater.* **2017**, 1700309.

[21] K. Li, R. H. Xie, W. K. Zhong, K. W. Lin, L. Ying, F. Huang, Y. Cao, *Sci. China Chem.* **2018**, *61*, 576.

[22] W. K. Zhong, K. Li, J. Cui, T. Y. Gu, L. Ying, F. Huang, Y. Cao, *Macromolecules* **2017**, *50*, 8149.

[23] S. S. Chen, S. Jung, H. J. Cho, N. H. Kim, S. Jung, J. Q. Xu, J. Oh, Y. Cho, H. Kim, B. Lee, Y. An, C. F. Zhang, M. Xiao, H. Ki, Z. G. Zhang, J. Y. Kim, Y. F. Li, H. Park, C. Yang, *Angew. Chem. Int. Edit.* **2018**, *57*, 13277.

[24] T. Kim, J. H. Kim, T. E. Kang, C. Lee, H. Kang, M. Shin, C. Wang, B. W. Ma, U. Jeong, T. S. Kim, B. J. Kim, *Nat. Commun.* **2015**, *6*, 8547.

[25] W. C. Zhao, S. Q. Zhang, Y. Zhang, S. S. Li, X. Y. Liu, C. He, Z. Zheng, J. H. Hou, *Adv. Mater.* **2018**, *30*, 1704837.

[26] F. Liu, S. Ferdous, E. Schaible, A. Hexemer, M. Church, X. D. Ding, C. Wang, T. P. Russell, *Adv. Mater.* **2015**, *27*, 886.

[27] X. D. Gu, Y. Zhou, K. Gu, T. Kurosawa, Y. K. Guo, Y. K. Li, H. R. Lin, B. C. Schroeder, H. P. Yan, F. Molina-Lopez, C. J. Tassone, C. Wang, S. C. B. Mannsfeld, H. Yan, D. H. Zhao, M. F. Toney, Z. N. Bao, *Adv. Energy Mater.* **2017**, *7*, 1602742.

[28] N. Shin, L. J. Richter, A. A. Herzing, R. J. Kline, D. M. DeLongchamp, *Adv. Energy Mater.* **2013**, *3*, 938.

[29] L. Ye, Y. Xiong, H. F. Yao, A. Gadisa, H. Zhang, S. S. Li, M. Ghasemi, N. Balar, A. Hunt, B. T. O'Connor, J. H. Hou, H. Ade, *Chem. Mater.* **2016**, *28*, 7451.

[30] L. Ye, Y. Xiong, Q. Q. Zhang, S. S. Li, C. Wang, Z. Jiang, J. H. Hou, W. You, H. Ade, *Adv. Mater.* **2018**, *30*, 1705485.

[31] K. Zhang, Z. M. Chen, A. Armin, S. Dong, R. X. Xia, H. -L. Yip, S. Shoaee, F. Huang, Y. Cao, *Sol. RRL* **2018**, *2*, 1700169.

[32] Y. B. Lin, S. Dong, Z. J. Li, W. H. Zheng, J. Y. Yang, A. L. Liu, W. Z. Cai, F. Liu, Y. F. Jiang, T. P. Russell, F. Huang, E. G. Wang, L. T. Hou, *Nano Energy* **2018**, *46*, 428.

[33] Y. Diao, Y. Zhou, T. Kurosawa, L. Shaw, C. Wang, S. Park, Y. K. Guo, J. A. Reinspach, K. Gu, X. D. Gu, B. C. K. Tee, C. H. Pang, H. P. Yan, D. H. Zhao, M. F. Toney, S. C. B. Mannsfeld, Z. A. Bao, *Nat. Commun.* **2015**, *6*, 7955.

[34] L. Ye, Y. Xiong, S. S. Li, M. Ghasemi, N. Balar, J. Turner, A. Gadisa, J. H. Hou, B. T. O'Connor, H. Ade, *Adv. Funct. Mater.* **2017**, *27*, 1702016.

[35] X. D. Gu, H. P. Yan, T. Kurosawa, B. C. Schroeder, K. L. Gu, Y. Zhou, J. W. F. To, S. D. Oosterhout, V. Savikhin, F. Molina-Lopez, C. J. Tassone, S. C. B. Mannsfeld, C. Wang, M. F. Toney, Z. A. Bao, *Adv. Energy Mater.* **2016**, *6*, 1601225.

[36] Z. Y. Li, L. Ying, R. H. Xie, P. Zhu, N. Li, W. K. Zhong, F. Huang, Y. Cao, *Nano Energy*, **2018**, *51*, 434.

[37] B. B. Fan, L. Ying, P. Zhu, F. L. Pan, F. Liu, J. W. Chen, F. Huang, Y. Cao, *Adv. Mater.* **2017**, *29*, 1703906.

[38] Z. Y. Li, R. H. Xie, W. K. Zhong, B. B. Fan, J. Ali, L. Ying, F. Liu, N. Li, F. Huang, Y. Cao, *Sol. RRL* **2018**, *2*, 1800196.

[39] Z. Y. Li, L. Ying, P. Zhu, W. K. Zhong, N. Li, F. Liu, F. Huang, Y. Cao, *Energy Environ. Sci.* **2019**, *12*, 157.

[40] Y. F. Wang, Z. L. Yan, H. Guo, M. A. Uddin, S. H. Ling, X. Zhou, H. M. Su, J. F. Dai, H. Y. Woo, X. G. Guo, *Angew. Chem. Int. Edit.* **2017**, *56*, 15304.

[41] H. You, D. Kim, H. H. Cho, C. Lee, S. Chong, N. Y. Ahn, M. Seo, J. Kim, F. S. Kim, B. J. Kim, *Adv. Funct. Mater.* **2018**, *28*, 1803613.

[42] D. Mori, H. Benten, H. Ohkita, S. Ito, K. Miyake, *ACS Appl. Mater. Interfaces* **2012**, *4*, 3325.

[43] K. D. Deshmukh, R. Matsidik, S. K. K. Prasad, L. A. Connal, A. C. Y. Liu, E. Gann, L. Thomsen, J. M. Hodgkiss, M. Sommer, C. R. McNeill, *Adv. Funct. Mater.* **2018**, *28*, 1707185.

[44] B. Friedel, C. R. McNeill, N. C. Greenham, Chem. Mater. **2010**, 22, 3389.

[45] Y. Zhou, T. Kurosawa, W. Ma, Y. K. Guo, L. Fang, K. Vandewal, Y. Diao, C. G. Wang, Q. F. Yan, J. Reinspach, J. G. Mei, A. L. Appleton, G. I. Koleilat, Y. L. Gao, S. C. B. Mannsfeld, A. Salleo, H. Ade, D. H. Zhao, Z. N. Bao, *Adv. Mater.* **2014**, *26*, 3767.

[46] T. Earmme, Y. J. Hwang, S. Subramaniyan, S. A. Jenekhe, *Adv. Mater.* **2014**, *26*, 6080.

[47] J. R. Moore, S. Albert-Seifried, A. Rao, S. Massip, B. Watts, D. J. Morgan, R. H. Friend, C. R. McNeill, H. Sirringhaus, *Adv. Energy Mater.* **2011**, *1*, 230.

[48] M. Schubert, D. Dolfen, J. Frisch, S. Roland, R. Steyrleuthner, B. Stiller, Z. H. Chen, U. Scherf, N. Koch, A. Facchetti, D. Neher, *Adv. Energy Mater.* **2012**, *2*, 369.

[49] N. J. Zhou, H. Lin, S. J. Lou, X. G. Yu, P. J. Guo, E. F. Manley, S. Loser, P. Hartnett, H. Huang, M. R. Wasielewski, L. X. Chen, R. P. H. Chang, A. Facchetti, T. J. Marks, *Adv. Energy Mater.* **2014**, *4*, 1300785.

[50] B. B. Fan, L. Ying, Z. F. Wang, B. T. He, X. F. Jiang, F. Huang, Y. Cao, *Energy Environ. Sci.* **2017**, *10*, 1243.

[51] L. Gao, Z. G. Zhang, L. W. Xue, J. Min, J. Q. Zhang, Z. X. Wei, Y. F. Li, *Adv. Mater.* **2016**, *28*, 1884.

[52] K. D. Deshmukh, T. S. Qin, J. K. Gallaher, A. C. Y. Liu, E. Gann, K. O'Donnell, L. Thomsen, J. M. Hodgkiss, S. E. Watkins, C. R. McNeill, *Energy Environ. Sci.* **2015**, *8*, 332.

[53] H. I. Kim, M. Kim, C. W. Park, H. U. Kim, H. K. Lee, T. Park, *Chem. Mater.* **2017**, *29*, 6793.

[54] H. P. Yan, B. A. Collins, E. Gann, C. Wang, H. Ade, C. R. McNeill, *ACS Nano* **2012**, *6*, 677.

[55] Z. J. Li, X. F. Xu, W. Zhang, X. Y. Meng, W. Ma, A. Yartsev, O. Inganas, M. R. Andersson, R. A. J. Janssen, E. G. Wang, *J. Am. Chem. Soc.* **2016**, *138*, 10935.

[56] X. M. He, F. Gao, G. L. Tu, D. Hasko, S. Huttner, U. Steiner, N. C. Greenham, R. H. Friend, W. T. S. Huck, *Nano Lett.* **2010**, *10*, 1302.

[57] C. McDowell, M. Abdelsamie, M. F. Toney, G. C. Bazan, *Adv. Mater.* **2018**, *30*, 1707114.

[58] H. C. Liao, C. C. Ho, C. Y. Chang, M. H. Jao, S. B. Darling, W. F. Su, *Mater. Today* **2013**, *16*, 326.

[59] J. Peet, N. S. Cho, S. K. Lee, G. C. Bazan, *Macromolecules* **2008**, *41*, 8655.

[60] C. J. Takacs, N. D. Treat, S. Kramer, Z. H. Chen, A. Facchetti, M. L. Chabinyc, A. J. Heeger, *Nano Lett.* **2013**, *13*, 2522.

[61] F. Liu, C. Wang, J. K. Baral, L. Zhang, J. J. Watkins, A. L. Briseno, T. P. Russell, *J. Am. Chem. Soc.* **2013**, *135*, 19248.

[62] B. A. Collins, J. E. Cochran, H. Yan, E. Gann, C. Hub, R. Fink, C. Wang, T. Schuettfort, C. R. McNeill, M. L. Chabinyc, H. Ade, *Nat. Mater.* **2012**, *11*, 536.

[63] S. R. Cowan, A. Roy, A. J. Heeger, *Phys. Rev. B* **2010**, *82*, 245207.

All-polymer solar cells fabricated via slot-die printing were obtained. In situ grazing incidence wide-angle X-ray scattering reveals the multiple crystallization kinetics during film drying. Printing with 1,8-diiodooctance leads to the formation of a multi-length-scale phase separation, and eventually improves the solar cell efficiency up to 9.10%, which is the highest efficiency for printed all-polymer solar cells.

Keywords: printing, slot-die, all-polymer solar cells, in situ characterization

Wenkai Zhong, Qin Hu, Yufeng Jiang, Yu Li, Teresa L. Chen, Lei Ying, Feng Liu,* Cheng Wang, Yi Liu, Fei Huang,* Yong Cao, Thomas P. Russell**

In Situ Structure Characterization in Slot-Die Printed All-Polymer Solar Cells with Efficiency Over 9%

ToC figure